Three-dimensional reconstruction for flame chemiluminescence field using a calibration enhanced non-negative algebraic reconstruction technique

Fuhao Zhang, Hujie Pan, Xuan Zhang, Xiongfei Bai, Zundi Liu, Xuesong Li *, Yuyang Li, Min Xu

School of Mechanical Engineering, Shanghai Jiao Tong University, Shanghai, 200240, China

ARTICLE INFO

ABSTRACT

The three-dimensional optical diagnostic method has received extensive attention from researchers because of its ability to provide three-dimensional physical information for reactive flow studies such as combustion. Computed tomography of chemiluminescence (CTC) has become a commonly used technique for three-dimensional, transient flame reconstruction purposes. However, due to view number limitations and considerable computational costs, the spatial resolution achieved and accuracy of the reconstruction are less satisfactory compared with applications such as in the medical fields. This investigation focuses on a few methods for improving the experimental and numerical performance of the CTC methods. Firstly, a cylindrical ChArUco calibration target was introduced and a multi-camera calibration method considering the position constraints of cameras was proposed to eliminate the registration error due to the rotation of the calibration target. Furthermore, a sub-voxel method was adopted to improve the spatial resolution of flame reconstructions. Finally, a non-negative algebraic reconstruction technique (NNART) was developed. The algorithm was verified with a simulated jet flame and then was tested against a diffusion jet flame and a swirl flame experimentally.

1. Introduction

In the current scientific research, two-dimensional optical diagnostic methods are still the mainstream for reactive flow studies, including high-speed photography, microscopic imaging, and laser-induced fluorescence. However, the physical quantities to be detected are naturally three-dimensional. Two-dimensional measurement methods will result in the loss of important three-dimensional information. To obtain the three-dimensional information, computed tomography of chemiluminescence (CTC) is currently widely adopted in 3D combustion and flame diagnostics. As a computational imaging approach, CTC uses multiple sensors/cameras at different viewing angles to obtain flame projections from various orientations simultaneously. Then, iterative reconstruction algorithms are used to reconstruct the volumetric flame in the sense of Radon transformation. The CTC technique has been well recognized by many investigations since it provides viable approaches for combustion mechanism analysis and transient and complex combustion characteristics [1–4]. During fuel combustion, intermediate radicals such as CH^*, OH^*, C_2^*, and CH_2O^* produce specific chemiluminescence at certain wavelengths [5]. If the soot formation inside the flame is negligible, the flame can be approximated as a transparent or translucent medium which light can propagate well through. With such assumptions, line-of-sight principles can be used, and the projection formed on the camera is an integrated signal along a certain light path [2,6–8]. CTC methods have been used to reconstruct volumetric distributions of flame emissions or flame temperatures [3,9]. As a passive and non-intrusive diagnostics method, CTC provides crucial experimental results for analysis or CFD validation purposes.

In typical CTC realizations, the volumetric domain of interest is usually discretized into voxels, as shown in Fig. 1. Commonly, the reconstruction process can be categorized into three stages, including camera view registration (calibration), weight matrix calculation, and iterative inversion. During camera view registration, the main purpose is to determine the intrinsic and extrinsic parameters of the cameras and address lens distortion, if there is any. Typical view registration for general imaging purposes can be achieved using chessboard methods [10,11]. The weight matrix represents the physical correlations between each voxel and pixels during the imaging process. More specifically, the weight matrix records the coefficient of light received by a specific pixel from a specific voxel through the optics. Such connections can be found using mathematical means such as calculating the point spread function and establishing the weight matrix in a forwarding scheme [9,12]. Researchers also used backward methods to build the weight matrix, in which ray tracing was adopted to calculate the intersection volumes between the light rays and specific voxels. Then, the weight matrix is built in a similar manner [13,14]. Establishing the weight matrix can be a computationally challenging task, and

---

* Corresponding author.
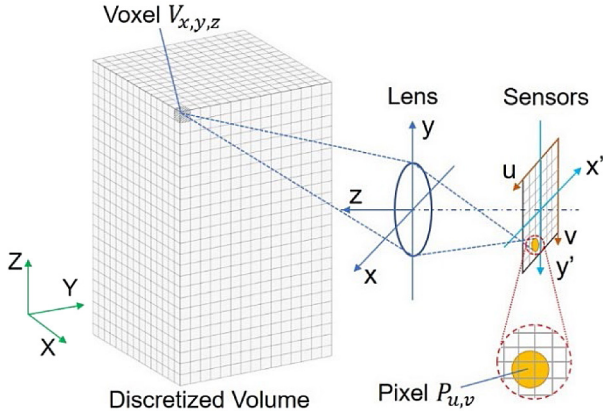*E-mail address:* xuesonl@sjtu.edu.cn (X. Li).

Fig. 1. Schematic of computed tomography of chemiluminescence. The flame region is discretized into cubic voxels represented by their coordinate indices. The flame intensity was then received by the cameras via the lens. The projections of a single voxel can be calculated using a sub-voxel projection scheme shown in Fig. 4, reflecting the need for camera calibration to build a proper weight matrix.

improper modeling of the light physics can induce notable errors in the reconstruction. Recently, there are also investigations that adopt deep learning methods to co-train the weight matrix and the three-dimensional flame luminosity from multiple flame projections [15, 16]. As for the reconstruction algorithm, since the CTC problem is a limited-view challenge, analytically inverting is not quite practical. The reconstruction itself can be regarded as a linear problem. Thus, global and non-linear algorithms are not required for reconstructions. Therefore, most of the CTC research conducted used iterative and deterministic algorithms such as the Algebraic Reconstruction Technique (ART) [17,18]. The basic idea of the ART method is to minimize the difference between the measured projections and calculated projections with an assumed flame intensity distribution. To improve the computational efficiency of ART methods, modifications were made to adjust the algorithm for different needs. This category of algorithms includes Simultaneous Algebraic Reconstruction Technique (SART) [19], Multiplicative Algebraic Reconstruction Technique (MART) [20,21], and SMART (Simultaneous MART) [22], etc. Although these methods are commonly used, their performance is not excellent in the aspect of computational speed and the RAM used. The reconstruction performance is also impacted when the number of views/effective pixels is insufficient in the experiment.

To further improve the fidelity of the CTC reconstruction, in this work, we firstly proposed a multi-camera calibration method designed specifically for tomographic reconstruction purposes, which uses a cylindrical ChArUco calibration target and utilizes the position constraints of cameras to improve the calibration accuracy. We also used parallelized sub-voxel projection schemes to improve calculation accuracy for the weight matrix. Furthermore, we re-derived the iteration governing equations in the ART method and proposed a Non-Negative Algebraic Reconstruction Technique (NNART). With this formality, no negative value would occur during intermediate tomographic reconstruction processes. The NNART algorithm was then further optimized to allow parallel computing in the form of the Simultaneous Non-Negative Algebraic Reconstruction Technique (SNNART). The performance of these techniques and methods was tested through numerical simulation and experimental validations in comparison to traditional techniques, as will be demonstrated in the following sections.

2. Methodology

2.1. Experimental setup

In this work, we used a maximum of ten cameras for the CTC reconstruction purposes, and the experimental setup is shown in Fig. 2.

In this study, no spectral filtering was made. Therefore, the flame chemiluminescence was directly captured by the cameras. The experimental setting is in agreement with our previous works [15,16]. To briefly introduce the imaging system settings, an image resolution of 1024×1280 was used across all cameras. The aperture was set with the aperture number 4.0 and an exposure time of 1 ms. All the cameras were installed onto a circular rail with a radius of 0.5 m, and the object distances can be adjusted by radial rails to achieve various observation conditions. The specific position parameters(distance and viewing angles) of each camera were obtained using the calibration method in Methodology Section, which can be found in Table 1. Before the CTC implementation, a linearity test for the cameras was performed with laser-induced fluorescence from Rhodamine 6G solutions, and the results were used as a look-up table to address any non-linearity of the camera response (although the responses were quite linear for each camera).

Two different types of flames were used in this study. The first flame used in this research is a methane-ethanol diffusion flame that approximates the reactor design in [23]. Methane flame was used as a purging flame with the flow rates of $CH_4:O_2:N_2$ = 1 slm: 2 slm: 3 slm (standard liter per minute). In the central zone, ethanol was injected at a flow rate of 5 ml/min and the nozzle diameter was 1.4 mm. The flow rate of the oxidizer (oxygen) was 5 slm. This flame can be used for fluctuating flame testing with a jet flame structure. The second flame was a turbulent swirl flame with a combustor outlet diameter of 37 mm. The combustor is equipped with a transparent quartz tube with an inner diameter of 135 mm and an outer diameter of 138 mm as the wall confinement. The height of the quartz tube was 200 mm. Swirl flames with and without the confinement were captured for reconstruction purposes. In the reconstruction of the swirl flame with a quartz tube, the method proposed by Liu et al. [24] was adopted to eliminate the imaging distortions caused by the light refraction of the quartz tube. The fuel used was methoxymethane (DME) and common air as the oxidizer. The equivalence ratio was 0.8, and the swirl number was 0.8 as well. Under the test conditions, the equivalence exit diameter of this reactor was 30 mm. The volumetric flow rate of the premixed gas was 150 L/min, which yielded an exit Reynolds number of 4790, and turbulent combustion was expected.

2.2. View registration

From the perspective of mathematics, the imaging process can be expressed as the mapping relationship from a volumetric domain (3D) onto a planar domain (2D). Assuming a specific point of $[X_w, Y_w, Z_w, 1]^T$ in the 3D domain would project onto a location $[u, v, 1]^T$ in the 2D domain, the mapping transition can be expressed by:

$$\begin{bmatrix} u \\ v \\ 1 \end{bmatrix} = sMT \begin{bmatrix} X_w \\ Y_w \\ Z_w \\ 1 \end{bmatrix} \tag{1}$$

Whereas M is the intrinsic matrix of the camera as a function of f_x, f_y, c_x, and c_y, which represents the focal lengths and imaging optical axis, respectively. T is the extrinsic matrix that describes the pose and the position of the camera, and s is the scaling coefficient. Besides, due to optical characteristics or flaws from the camera lens or imaging system, the camera imaging process might suffer from distortions [25]. The distortion of the camera primarily consists of radial distortion and tangential distortion. Assuming the pixel coordinates before distortion are $[x, y]^T$ and after distortion $[x_d, y_d]^T$, then we have:

$$\begin{bmatrix} x_d \\ y_d \end{bmatrix} = (1 + k_1 r^2 + k_2 r^4 + k_3 r^6) \begin{bmatrix} x \\ y \end{bmatrix} + \begin{bmatrix} \Delta x_t \\ \Delta y_t \end{bmatrix} \tag{2}$$

$$\begin{bmatrix} \Delta x_t \\ \Delta y_t \end{bmatrix} = \begin{bmatrix} 2p_1 xy + p_2 (r^2 + 2x^2) \\ 2p_1 (r^2 + 2y^2) + 2p_2 xy \end{bmatrix} \tag{3}$$
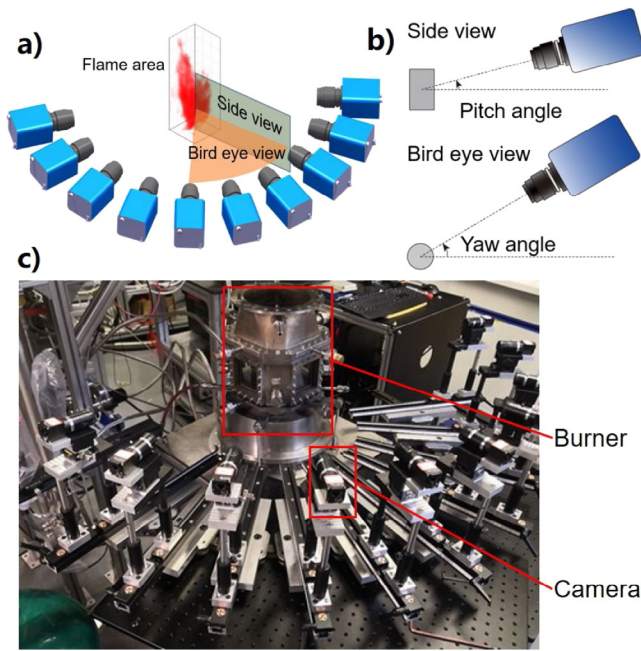
Fig. 2. Experimental setup of the co-planar computed tomography of chemilumines-cence. A total of 10 cameras were used in the experiment. Panel (a). Schematic of the multicamera imaging system for CTC. Panel (b). Explanations of viewing angles for the cameras. Panel (c). Experimental setup for flame reconstruction. Detailed projection parameters of each camera can be found in Table 1.

Fig. 3. Schematic of ChArUco (Chessboard + ArUco) and the corresponding calibration object. Panel (a). ChArUco formation. Panel (b). The cylindrical ChArUco calibration target for experiments. Panel (c). Post-processed image for view registration. Panel (d). Bird-eye view of the cylindrical ChArUco calibration target. Panel (e). Post-processed image for the bird-eye view of calibration target.

where $r^2 = x^2 + y^2$, (k_1, k_2, k_3) are radial distortion coefficients, and (p_1, p_2) are tangential distortion coefficients, respectively. The camera calibration process is aimed to find these coefficients and parameters to fully describe the imaging system.

Usually, the calibration process can be done with a black and white chessboard, and customized programs (i.e., based on OpenCV [26]) can be used to detect corner points to achieve the sought parameters of the cameras [10]. In the chessboard calibration process, it is the premise for calibration implementation to detection of all the corner points on the chessboard plate correctly, because the coordinates of these corner points are identified according to the relative positional relationship among the corner points. However, for tomographic applications, since many cameras surrounding the target area are required to be calibrated simultaneously, it would be challenging for the cameras viewing the side of the calibration plate to acquire accurate calibration parameters. Under an undesirable viewing angle, the detection of corner points on the chessboard is prone to large errors, resulting in large calibration errors or even calibration failure, which limits the angle distribution of cameras to a certain extent. One potential solution is to rotate the cali-bration plate for the other cameras, but such acts would introduce more uncertainties during the calibration, i.e., the exact posing variation of the calibration plate during the rotation.

In this work, we proposed a novel multi-camera calibration method for CTC applications based on ChArUco. ChArUco is a combination of ArUco [27,28] and chessboard. ArUco is a type of QR code for identification purposes, and ChArUco embedded ArUco codes into the chessboard so that the corner points can be identified according to the corresponding ArUco markers, as can be seen in Panel (a) of Fig. 3. There are existing ChArUco studies [29,30], but the calibration target is still a plate. In this study, we employed a cylindrical ChArUco calibration target (see Panel (b) and Panel (c) of Fig. 3) and it does not need to detect all the corner points in the process of calibration. The bird-eye view of the calibration target is shown in Panel (d) and Panel (e). Thus, cameras can be arranged in a 360-degree range surrounding the target reconstruction area.
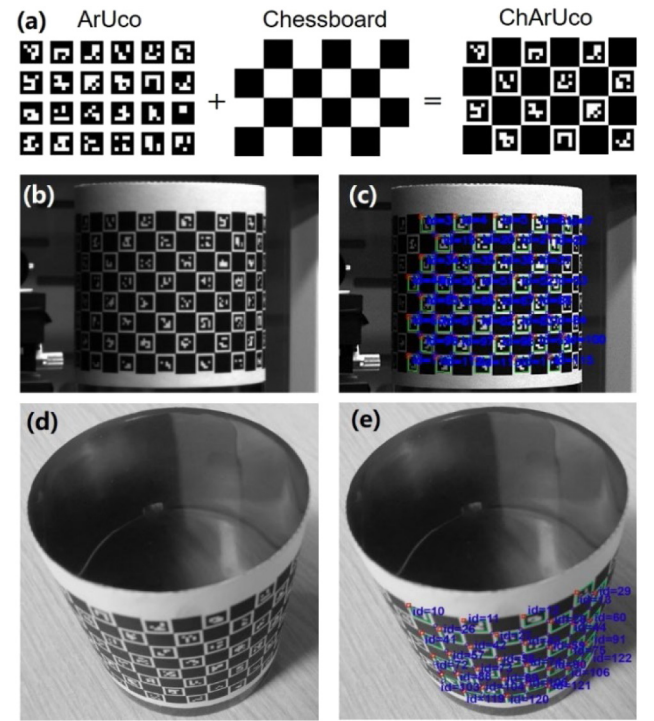
During the calibrations, multiple cameras simultaneously acquired the cylindrical calibration target's images in different locations and orientations, and the cylindrical coordinates of the ChArUco target's corners were used in the program. Note that for a fixed camera, the intrinsic parameters remain unchanged for its captured images, but the extrinsic parameters are estimated based on the world coordinate system fixed on the calibration target. After getting the coordinate pairs of corner points in the imaging plane and three-dimensional space, the intrinsic parameters of cameras can be obtained through the method proposed by Z. Zhang [10], and then the extrinsic parameters can be estimated in the sense of Perspective-N-Point (PNP) [31], for which we adopted the solvePnP function in OpenCV [26] to obtain the parameters sought. Since this calibration method can be applied to both chessboard and cylindrical ChArUco, comparable calibration accuracy can be achieved by these two calibration targets, while the cylindrical ChArUco relaxes the requirements for viewing angles and performs better at undesirable viewing angles. The comparison of the calibration results between the chessboard and cylindrical ChArUco is demonstrated in the Result and Discussion Section as follows.

However, due to the influence of noise, the calibration accuracy obtained by the above-mentioned method is still at a relatively lower level. We noticed that the positions of cameras are fixed in the multi-camera imaging system. Although the position of the calibration target will change during the calibration process, the form of the position change should be consistent for each camera, which is called the relative position constraints of cameras. In this paper, we proposed a method that utilizes the relative position constraints of cameras to further improve the calibration accuracy. A rotation matrix R and a translation vector t are used to represent the transformation between two positions of the calibration target. Taking the coordinate system fixed on the calibration target at the 0th position as a reference, the three-dimensional coordinate of the corner point on the calibration

target at the ith position can be expressed as:

$$Q_{i \to 0} = R_i Q_i^k + t_i \qquad (4)$$

Whereas Q_i^k is the three-dimensional coordinate of the corner point on the calibration target at the ith position and $Q_{i \to 0}$ is the coordinate of the same corner point in the coordinate system fixed on the calibration target at the 0th position. The subscript k indicates that the corner point is detected by the kth camera. The rotation matrix R_i is expressed by three Euler angles and the translation vector t_i is expressed by the displacements along the x, y, and z axis. In this way, all the corner points on the calibration target at different positions can be translated to the same three-dimensional coordinate system. The coordinates of the projected corner points on the imaging plane of the kth camera can be calculated as:

$$\tilde{q}_i^k = H_0^k Q_{i \to 0} \qquad (5)$$

where $\tilde{q}_i^k$ is the calculated coordinate of projected corner point on the kth camera's imaging plane and the calculated corner point belongs to the calibration target at the ith position. H_0^k is the homography matrix of the kth camera and $H_0^k = sM^k T_0^k$. M^k is the intrinsic matrix of the kth camera, and T_0^k is the extrinsic matrix which describes the position and orientation of the kth camera in the coordinate system fixed on the calibration target at the 0th position. Therefore, $\tilde{q}_i^k$ can be obtained according to Ep. (4) and Eq. (5) as:

$$\tilde{q}_i^k = H_0^k \left(R_i Q_i^k + t_i \right) \qquad (6)$$

Then the multi-camera calibration task can be transformed into a minimum optimization problem:

$$min \quad l = \sum_k \sum_i \left\| H_0^k \left(R_i Q_i^k + t_i \right) / \tilde{b}_i^k - q_i^k \right\|_2^2 \qquad (7)$$

where $\tilde{b}_i^k$ is the third component of homogeneous coordinate, q_i^k is the measured coordinate of corner point on imaging planes. A gradient descent strategy was applied to solve this nonlinear optimization problem. To avoid the iterative process falling into a local minimum, we used the results of the above-mentioned calibration method without position constraints to initialize H_0^k, and adopted the average results of pose estimation by each camera individually to initialize R_i and t_i. The popular deep learning framework PyTorch [32] was used to implement the calibration method and Adam (Adaptive Moment Estimation) [33] was chosen as the optimization algorithm. In the process of optimization calculation, the exponential decay rates of Adam algorithm were set to $\rho_1 = 0.9$, $\rho_2 = 0.999$ as default and the step factor $\varepsilon = 0.001$. The progress where all the detected corner points participate in the calculation once is considered as a complete iteration, and the number of iterations was set to 50. The addition of cameras' position constraints will significantly improve the calibration accuracy of the multi-camera imaging system, which is of significant importance for improving the calculation accuracy of the weight matrix and thus the flame reconstruction accuracy. The calibration results are incorporated in the Result and Discussion Section as follows.

2.3. Reconstruction algorithm

Before the flame reconstruction process, the weight matrix needs to be established to correlate emission intensity and projections onto the cameras. As required by the reconstruction algorithms, the weight matrix is needed to link each voxel and pixel, and such a relationship is usually based on a one-step calculation from a single voxel to multiple pixels. However, projecting a cubic voxel onto the CCD chip based on very simple models and geometries (such as the pinhole model) can induce non-negligible error. To achieve higher accuracy in establishing the weight matrix, in this work, we adopted a sub-voxel projection scheme, as shown in Fig. 4. In our sub-voxel model, each voxel was discretized into $50 \times 50 \times 50$ sub-voxels and the projection of each voxel is calculated. Then the projection contribution of this voxel is
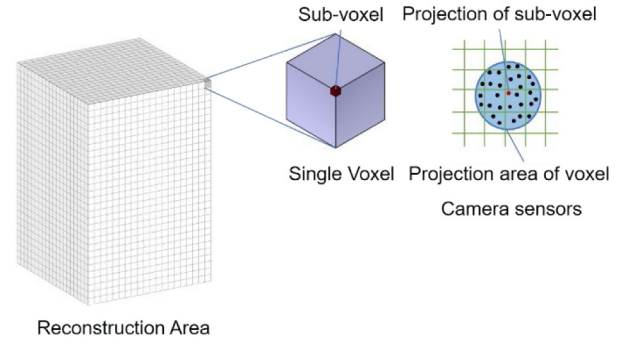

Fig. 4. Schematic of sub-voxel projection. The detailed imaging relationship between voxels and pixels can be found in Fig. 1.

statistically found from the sub-voxels. Increasing sub-voxel divisions is beneficial to the improvement of reconstruction accuracy. However, as the number of sub-voxels increases, its effect on the reconstruction accuracy will gradually weaken, and the requirements for computing resources will increase sharply at the same time. So, the determination of sub-voxel divisions requires a trade-off between reconstruction accuracy and computational complexity. And the number of sub-voxel divisions in the experiment needs to be determined according to the specific imaging settings. In our experiments, the projection of a single voxel covers an area of approximately 5×5 pixels. We have checked the weight matrix with various sub-voxel settings (10, 20, 50, and 100), and we found that $50 \times 50 \times 50$ sub-voxels can compromise the accuracy and the computational cost. The sub-voxel mode was only used for weight matrix calculation and not for reconstruction to reduce the size of the weight matrix. As such, we used this sub-voxel setting in CTC reconstructions. The computational cost is expected to grow higher with the sub-voxel setting, so we adopt GPU parallel computing to accelerate the computational efficiency for the purpose of weight matrix calculation. We used an RTX 2080Ti graphic card for parallel weight matrix computation. With a $60 \times 60 \times 220$ flame discretization and $50 \times 50 \times 50$ sub-voxels, the computational cost using a GPU card is roughly less than 0.5 h, compared to 5 h using an i9 10900x CPU (3.70 GHz), which is acceptable in practical applications.

For CTC applications, the algebraic reconstruction technique (ART) [17,18] is commonly used to solve the problem in an iterative approach. The ART algorithm finds the flame reconstructions by minimizing the difference between the simulated projections and the measured projections. The voxel values are updated by each pixel, then each view after iterating all the pixels from one view. However, the computational cost of iterating each pixel one-by-one would be very high. Therefore, the simultaneous algebraic reconstruction technique (SART) [19] was proposed to update the voxels from a complete projection simultaneously. The mechanism of SART can be expressed by:

$$x^{j+1} = x^j + \mu W^T D^2 \left(b - W x^j \right) \qquad (8)$$

Where x^j is the structured voxel vector after the jth iteration, b is the structured projection vector, W is the weight matrix, and μ is the relaxation coefficient. D is defined as $diag\left(1/\|w_1\|_2, 1/\|w_2\|_2, \ldots, 1/\|w_p\|_2 \right)$, where $\|w_i\|_2$ is the 2-norm of the vector composed of elements in the ith row of W. In this manner, the whole view can be updated in a matrix form. While although ART and SART algorithms can achieve good robustness and reconstruction accuracy, their convergence speeds are not quite desirable. There are also reconstruction glitches/streaks seen and reported in ART and SART reconstructions due to the nature of the algorithms [16,34]. One potential reason for this drawback is that in the application of CTC, negative flame luminosity is physically impossible, but the reconstruction algorithm itself does not incorporate corresponding constraints for this physical implication. To introduce

the non-negative constraints, we proposed a non-negative algebraic reconstruction technique (NNART) in this work and introduced the intermediate parameter as follows:

$$y_v^2 = x_v \tag{9}$$

Therefore, this reconstruction has converted into minimizing $\Delta = \left(b_p - w_p^T y^2\right)$, in which the vector y can be expressed by $y^2 = [y_1^2, y_2^2, \ldots, y_v^2]^T = [x_1, x_2, \ldots, x_v]^T = x$. Based on this formulation, to perform an iterative reconstruction, the gradient of the newly defined variables is expressed as follows:

$$\partial\Delta/\partial y_v = -4w_{pv}y_v\left(b_p - w_p^T y^2\right) \tag{10}$$

Therefore, in the sense of the ART algorithm, the iterative reconstruction process can be modified as in Eq. (11):

$$y_v^{j+1} = y_v^j + \mu w_{pv}y_v^j\left[b_p - w_p^T\left(y^j\right)^2\right] / \left[\left(w_p^2\right)^T\left(y^j\right)^2 + \alpha\right] \tag{11}$$

In which $w_p^T\left(y^j\right)^2 = \sum_v w_{pv}\left(y_v^j\right)^2$, $\left(w_p^2\right)^T\left(y^j\right)^2 = \sum_v \left(w_{pv}y_v^j\right)^2$, $\alpha = max_p\left(w_p^2\right)^T I^2 = max_p \left\|w_p\right\|_2^2$. The addition of α is to stabilize the reconstruction procedure. In this approach, the non-negative constraints have been incorporated into the ART algorithm. It should be noted that, similar to the MART mentioned above, since the voxel values will participate in the calculation in the form of product during the NNART update process, it is necessary to initialize the voxel vector with non-zero values during initialization. To further accelerate the NNART algorithm, we derived analytically and Eq. (8) can be rewritten into the forms as shown in Eqs. (12) and (13):

$$y^{j+1} = y^j + \mu K^T\left[\left(D'\right)^2 + A\right]\left[b - W\left(y^j\right)^2\right] \tag{12}$$

$$K = \begin{pmatrix} w_{11}y_1^j & w_{12}y_2^j & \cdots & w_{1v}y_v^j \\ w_{21}y_1^j & w_{22}y_2^j & \cdots & w_{2v}y_v^j \\ \vdots & \vdots & \ddots & \vdots \\ w_{p1}y_1^j & w_{p2}y_2^j & \cdots & w_{pv}y_v^j \end{pmatrix} \tag{13}$$

Where the matrix $D' = diag\left(1/\left\|k_1\right\|_2, 1/\left\|k_2\right\|_2, \ldots, 1/\left\|k_p\right\|_2\right)$, $A = diag\left(1/\alpha, 1/\alpha, \ldots, 1/\alpha\right)$ with the non-negative structure. We will not explicate the derivation process and will show reconstruction algorithm verification in the section that follows. With these modifications and derivations, we expect that the reconstruction algorithm would be more efficient with fewer streaks present in the flame reconstructions.

3. Results and discussions

3.1. View registrations

We firstly demonstrate the comparison of calibration results between the chessboard and cylindrical ChArUco, as shown in Fig. 5. In this case, the calibration algorithm without position constraints of cameras was adopted for the chessboard and cylindrical ChArUco calibration separately. And the calibration results considering position constraints will be demonstrated later. Panel (a) of Fig. 5 shows the calibration process using a single and fixed calibration plate. As can be seen, a clear and complete view of the calibration plate can be captured by the fifth camera, but due to the difference in viewing angle, View 10 captured only a small and distorted calibration plate. The view of the calibration plate would be even worse if the actual view is perpendicular to the view orientation of View 5. Panel (b) shows the calibration using the ChArUco calibration cylinder. As can be seen, the calibration target projected onto different cameras shows similar projection outcomes with satisfactory imaging quality, and the ArUco codes embedded can be used to assist in identifying the corner points during calibration. Panel (c) of Fig. 5 depicts the registration error from
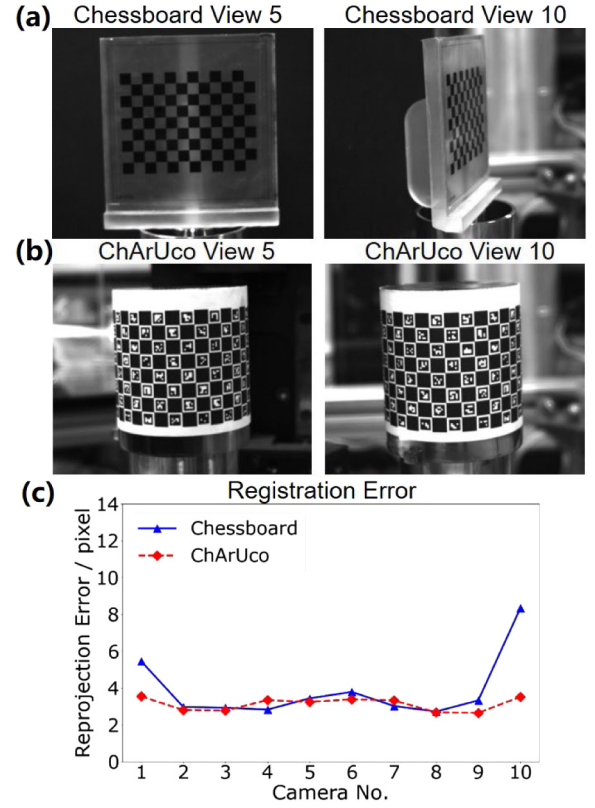

Fig. 5. Comparison of chessboard calibration and ChArUco calibration (without position constraints of cameras). Column (a). View 5 and View 10 calibration images using a chessboard pattern. Panel (b). View 5 and View 10 calibration images using a ChArUco target. Panel (c). Comparison of performance.

chessboard calibration and ChArUco calibration, respectively. We use the reprojection error as the registration error metric, which is obtained by:

$$E_{repro} = \sum_i \left\|\widetilde{p}_i - p_i\right\|_2 / n \tag{14}$$

where $\widetilde{p}_i$ is the calculated projection coordinate and p_i is the measured coordinate of ChArUco corner points on images. n is the number of detected corners. As can be seen, ChArUco generally keeps equivalent accuracy compared with chessboard calibration but generates much better results for View 10 since the corner points detected in View 10 is not satisfactory. As shown in Fig. 5, the cylindrical ChArUco can achieve comparable calibration accuracy as the chessboard method while ensuring the quality of corner detection under each viewing angle, so the cylindrical ChArUco is more suitable for multi-camera calibration.

To further improve the calibration accuracy of the multi-camera imaging system, the position constraints of cameras were considered in the calibration process, as described in the Methodology section. During the calibration, we used 10 cameras to simultaneously capture 36 positions of the cylindrical ChArUco calibration target. We kept 80% of the detected corner points for the calibration parameters calculation and 20% for calculating the reprojection error as the calibration accuracy index. The calibration results with and without position constraints are shown in Fig. 6. In the case without position constraints, the calibration of each camera was performed independently and there are no connections among cameras during the calibration process. It results in the inconsistency in pose estimation for the calibration target among different cameras and causes a relatively larger calibration error. The overall reprojection error is about 3.5 pixels. This means a measurement error of about 0.4 mm in our imaging system. After using

Table 1
Camera calibration parameters.

| Camera NO.	Camera intrinsic parameters		Camera extrinsic parameters	
	Camera matrix parameters $[f_x/10^3, f_y/10^3, c_x/10^2, c_y/10^2]$	Distortion coefficients $[k_1, k_2, p_1/10^{-3}, p_2/10^{-3}, k_3]$	Rotation [Pitch, Yaw, Roll] (°)	Translation $[T_x, T_y, T_z]$ (mm)
1	[2.154, 2.152, 6.400, 5.120]	[−0.101, −0.458, −1.027, −4.234, 8.211]	[−16.875, −81.423, 17.351]	[75.847, −333.698, 21.039]
2	[2.154, 2.160, 6.400, 5.120]	[−0.087, −0.574, 4.160, 1.551, 4.839]	[−0.994, −63.971, 0.846]	[172.768, −303.791, 12.310]
3	[2.146, 2.145, 6.400, 5.120]	[−0.059, −1.250, −0.931, 0.112, 12.990]	[−2.413, −46.273, 0.899]	[253.763, −247.686, 11.758]
4	[2.147, 2.147, 6.400, 5.120]	[−0.061, −0.636, −0.504, 1.258, 5.169]	[−3.507, −29.780, 0.541]	[311.807, −170.632, 16.758]
5	[2.145, 2.145, 6.400, 5.120]	[−0.101, −0.449, 2.468, −2.213, 4.122]	[−4.039, −12.693, −0.674]	[323.856, −84.514, 27.388]
6	[2.152, 2.151, 6.400, 5.120]	[−0.090, −0.392, −0.555, −1.323, 0.825]	[−3.579, 1.249, −1.798]	[317.174, −1.650, 30.799]
7	[2.142, 2.142, 6.400, 5.120]	[−0.088, −0.603, −0.019, −1.468, 6.140]	[−4.838, 15.437, −2.900]	[313.124, 83.250, 33.7862]
8	[2.147, 2.146, 6.400, 5.120]	[−0.105, 0.333, −0.130, −1.057, −5.948]	[−5.083, 30.844, −4.869]	[281.486, 153.840, 35.259]
9	[2.146, 2.146, 6.400, 5.120]	[−0.064, −0.589, 5.092, −1.010, 6.005]	[−9.112, 44.897, −8.739]	[228.619, 223.997, 39.761]
10	[2.144, 2.143, 6.400, 5.120]	[−0.043, −3.031, −2.579, −2.233, 22.004]	[−10.224, 59.867, −10.739]	[154.675, 278.879, 41.360]
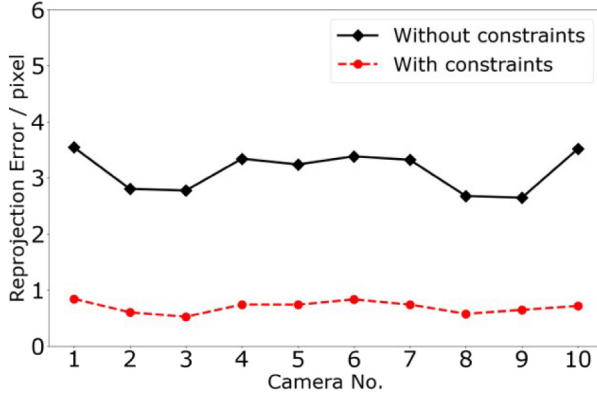
Fig. 6. Comparison of calibration accuracy with and without position constraints of cameras.

the calibration method considering the position constraints of cameras, the positional relationship between cameras has been well regularized. The reprojection error was significantly reduced to less than 1 pixel (0.1 mm accuracy level), which is of great significance for improving the performance of flame reconstruction. In this investigation, we used the cylinder ChArUco calibration method considering camera position constraints to acquire all intrinsic and extrinsic parameters of cameras, and these values are incorporated in Table 1.

3.2. Numerical verifications

With the camera parameters achieved from experiments, we firstly used these parameters as camera characteristics for numerical verifications. In the verification, we used a synthetic jet flame discussed in [15], and we will not explicate the phantom specifics in this work. We used a $60 \times 60 \times 220$ spatial discretization, and different algorithms were used to test their capabilities. Representative reconstruction slices and the ground truth are shown in Fig. 7. Panel (a) of Fig. 7 shows the scalar distributions of the flame at different vertical locations, and Panel (b) represents the reconstruction error using the structural similarity (SSIM), defined as follows:

$$SSIM(x, y) = \frac{(2\mu_x\mu_y + c_1)(2\sigma_{xy} + c_2)}{(\mu_x^2 + \mu_y^2 + c_1)(\sigma_x^2 + \sigma_y^2 + c_2)} \quad (15)$$

The detailed definition of SSIM can also be found in [35]. SSIM is calculated by comparing the pixel values in a small window at the same location of the two images. In Eq. (15) μ_x and μ_y are the mean values of the pixels in the small window and σ_{xy} is the covariance of the pixel values from the two windows, σ_x and σ_y are the variances of the pixel values in the windows of the two images respectively. Constants c_1 and c_2 are added to avoid numerical instability. Their values were set as default in the literature: $c_1 = (0.01L)^2$ and $c_2 = (0.03L)^2$ in which L

is the dynamic range of the image and is set as one since the volume flames were normalized before the comparisons. In brief, the higher the SSIM is, the closer the computed result is compared to the ground truth.

To illustrate the performance of different algorithms, we added a 10% relative Gaussian noise (with respect to the average signal strength of each pixel of the projection) to the measurement. Due to the differences in mechanism between serial and parallel algorithms, the numbers of iterations required are different. In this work, we set the number of iterations to 60 for serial reconstruction methods (ART and NNART) and 100 for parallel methods (SART and SNNART). With this computational cost, the reconstructions were converged based on a preset criterion. As seen from Panel (a) of Fig. 7, all reconstruction algorithms reconstructed the synthetic jet flame. However, under high noise conditions, notable streaks were seen for ART and SART reconstructions, which are also clearly spotted in Panel (b) of Fig. 7. Although the streak feature might somehow be suppressed by regularizations, regularizations would inevitably alter/skew reconstruction based on projections. In comparison, NNART and SNNART methods generate more satisfactory results with less notable reconstruction streaks seen at different horizontal planes. Furthermore, the reconstructions in the vertical planes by various reconstruction algorithms are shown in Fig. 8, and SSIMs are demonstrated as well. As can be seen, ART and SART algorithms accumulate notable errors at flame edges, which is partially due to the error induced by the streaks. In comparison, smaller error/ better SSIM agreements are seen when NNART or SNNART algorithm is adopted.

Such comparisons justify the modified forms shown in Eqs. (9)– (13) and also verified that the NNART algorithm is superior to the ART algorithm in handling CTC problems. It should be noted that the computational cost of NNART methods is slightly higher than ART methods. It took the NNART method 31 min for one iteration and 28 min for ART algorithms. For algorithms in the simultaneous form, it took SNNART 9.5 s for one iteration and 7.8 s for the SART methods. We hold that the computational costs of NNART and ART are on the same level, but NNART converges faster than ART (thus saving the computational cost), as will be stated as follows.

We then examined the reconstruction accuracy and convergence speed for different algorithms, as shown in Fig. 9. We used the cosine distance between the calculated result and ground truth as the reconstruction accuracy index, and the residual between two consecutive iterations as the convergence performance index. Panel (a) and Panel (c) compare the cosine distance as a function of iterations, and Panel (b) and Panel (d) compare the residual as a function of iterations, respectively. As can be seen, both cosine distance and residual using the NNART methods converge much faster and declined to a lower value compared with ART methods, which means that the NNART method converges faster than the ART method, while maintaining a lower level of reconstruction error (cosine distance). Therefore, we hold that the weak non-negative constraint added has notably improved the computational performance of CTC, given no negative flame luminosity exists as a fact.
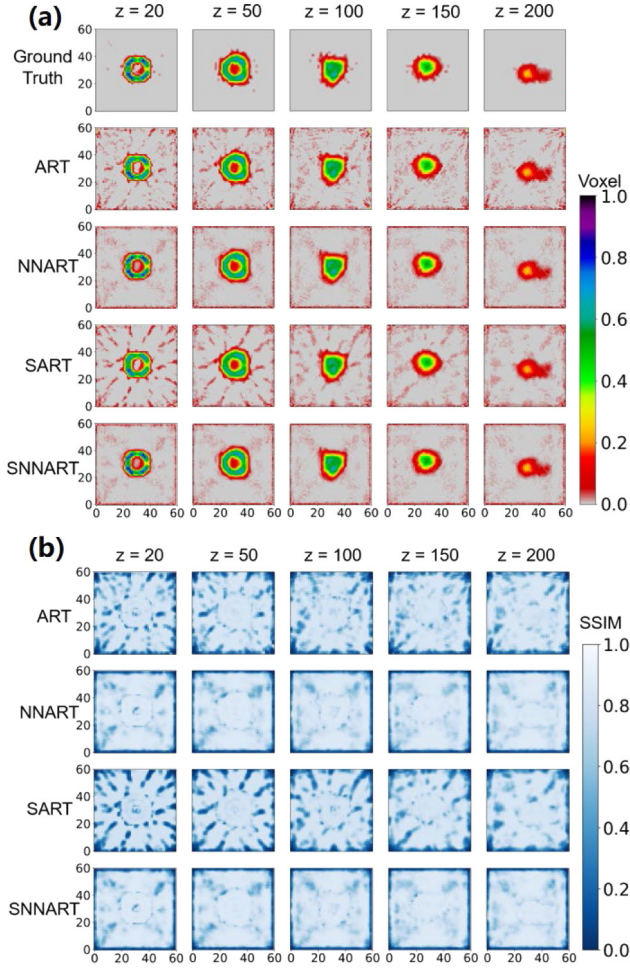
Fig. 7. Horizontal slices from 3D reconstructions using a synthetic jet flame phantom. Panel (a). Reconstruction results using ART, NNART, SART, and SNNART, respectively (The color bar was processed to emphasize streaks). Panel (b). Calculated SSIM for each method.
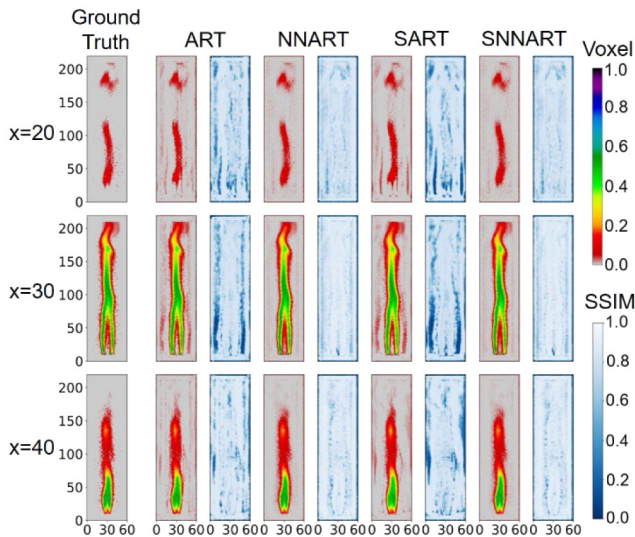

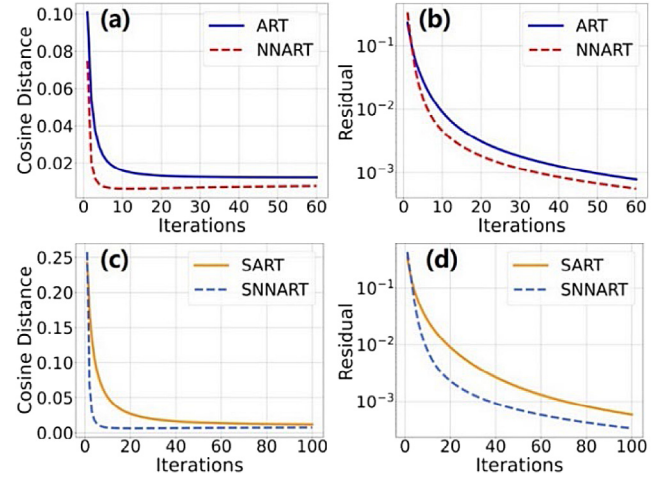**Fig. 8.** Vertical slices from 3D reconstructions using a synthetic jet flame phantom.

Fig. 9. Comparison of the convergence speed for different algorithms. Panel (a). Cosine distance, ART vs. NNART. Panel (b). Residual, ART vs. NNART. Panel (c). Cosine distance, SART vs. SNNART. Panel (d). Residual, SART vs. SNNART.

3.3. Experimental validation and discussion

In this section, we present the results obtained using the SNNART algorithm and perform some analysis on this basis, and then attach the performance comparison with SART. We firstly analyze the methane-ethanol diffusion flame, and the results are shown in Fig. 10. For this specific flame, ethanol is atomized, then mixed with methane and combusted; therefore, the diffusion combustion is quite unstable and fluctuating. For this reconstruction purpose, we used a $100 \times 100 \times 250$ reconstruction spatial discretization with a spatial resolution of 0.5 mm. Due to the complexity of the flame structure, we used a $50 \times 50 \times 50$ sub-voxel setting to compute the weight matrix. The exposure time of the cameras was set to 0.1 ms. The reconstructed flame was rendered volumetrically to illustrate local intensities and the spatial structure. As can be seen, with the settings described, we succeeded in reconstructing the jet flame with both macroscopic and microscopic features of the flame preserved. The reconstructed height of the flame was 120 mm, and the maximum radius of the jet flame was 22 mm. Furthermore, we can clearly identify each stage of the diffusion jet flame from injection to the formation of the vortex structure at the leading edge of the flame. Distinctive flame sheets (i.e. the hollow features near $z = 50$) and flame wrinkling can be captured by the flame reconstruction, which verifies the performance of the SNNART reconstruction.

Next, we continue to investigate the implementation of SNNART in swirl flame reconstruction. We used a $150 \times 150 \times 200$ reconstruction spatial discretization (considering the actual size of the flame) with a spatial resolution of 1.0 mm. We also used a $50 \times 50 \times 50$ sub-voxel setting to compute the weight matrix for enhanced accuracy. The exposure time of the cameras was set to 1 ms. No quartz tube was added in this test. Corresponding representative flame results are shown in Fig. 11. From the reconstruction results, we can identify a vortex structure inside the swirl flame, which is known as the processing vortex core phenomenon associated with the swirl flame. Such a performance further attests to the capability of the proposed SNNART method, as well as CTC modifications and improvements introduced in previous sections. The reconstructed flame height was 199 mm and the maximum flame radius 38 mm, respectively. Similar to the jet flame reconstruction, fine flame structures, and details can be seen in the swirl flame reconstruction. The ratio of the surface area and total flame volume was 0.14/voxel size, which was much smaller than that of the diffusion jet flame (1.07/voxel size), which indicates that the swirl flame is simpler than the diffusion flame in the aspect of the flame structure.
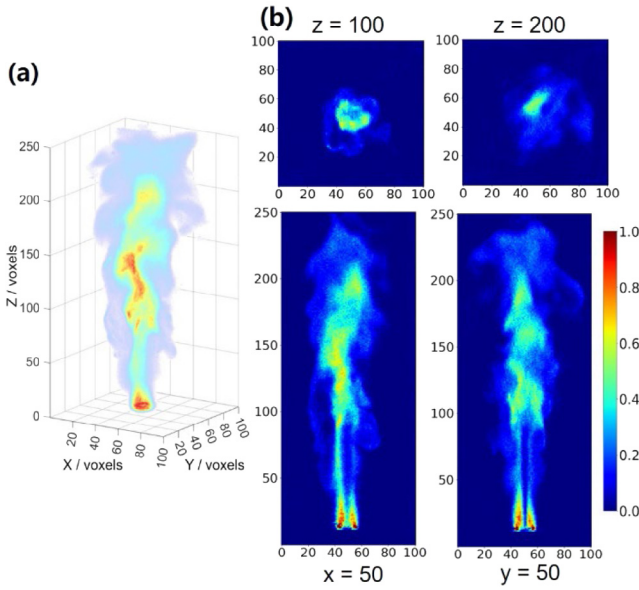
Fig. 10. Experimental reconstruction results of the diffusion flame. Panel (a). 3D flame reconstruction visualization. (b). Vertical and horizontal slices of the reconstructed flame.
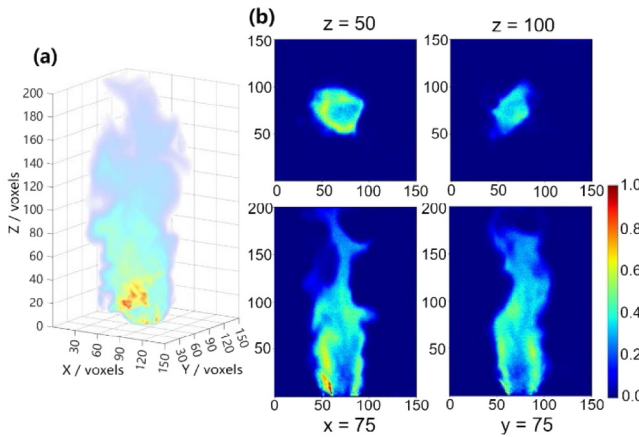

Fig. 11. Experimental reconstruction results of the swirl flame without the quartz tube. Panel (a). 3D flame reconstruction visualization. (b). Vertical and horizontal slices of the reconstructed flame.

Fig. 12. Experimental reconstruction results of the constrained swirl flame with the quartz tube. Panel (a). 3D flame reconstruction visualization from different view orientations. (b). Vertical and horizontal slices of the reconstructed flame.

Fig. 12 continues to explore the swirl flame with the quartz tube incorporated. To avoid imaging distortions due to the refraction of the optical rays across the curved wall of the quartz tube, we used the method proposed by Liu, H et al. [24] to eliminate the imaging distortions caused by the quartz tube. As can be seen in Fig. 12, the swirl flame was more apparent when the reactions and flows were constrained inside the quartz tube. Panel (a) of Fig. 12 exhibits the flame reconstruction from different view orientations, and a swirling pattern can be clearly identified. Panel (b) of Fig. 12 shows the flame reconstruction slices at different locations, which demonstrates many significant features of the swirl flame. Firstly, for the horizontal slice at $z = 100$, it can be seen that the reconstruction flame was limited in a circular regime, and the diameter of this circle matched the inner diameter of the quartz tube. Such results mean that the flame has filled the quartz tube completely at this location. At $z = 50$, it can be seen that the swirl flame was stopped by the quartz tube on the left-hand side, but the flame had not propagated to the right-hand side yet. A circular flame pattern is also evident at this location. In the vertical flame slices, notable vortex streets could be seen on both sides of the flame in the
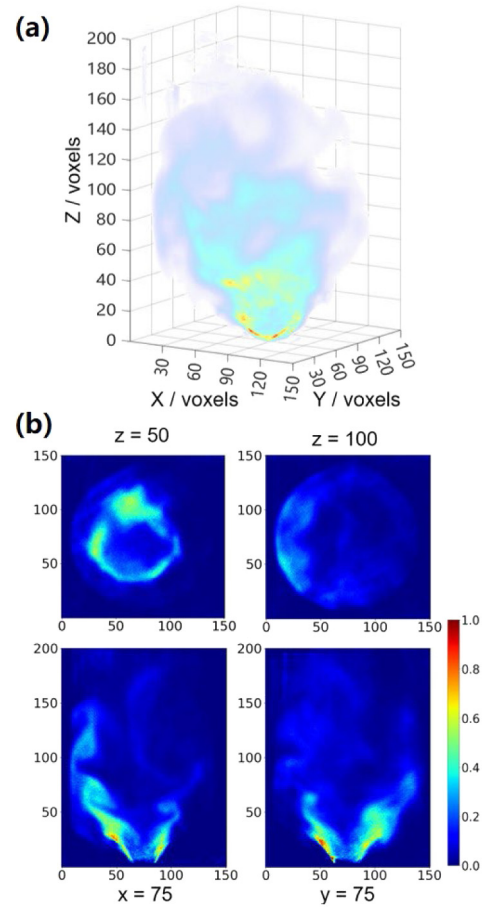
flame wake region, which also justified the SNNART algorithm had a superior capacity for practical CTC applications.

Fig. 13 depicts a flame structure analysis from the results shown in Fig. 12 by plotting an iso-surface plot at a specific flame intensity value, as seen in Panel (a). It can be seen that this flame structure can be regarded as the precessing vortex core, which is a distinctive feature of swirl flames. Although we only present the flame reconstruction at a specific timing, the precessing vortex core was seen in almost all constrained swirl flame reconstructions using SNNART. Multiple vortices could be seen in the same flame reconstruction, as seen in Panel (b) of Fig. 13 (the flame vortices were denoted by yellow dash lines). From the existing literature, the swirling frequency could be inferred from flame dimensions [36]. In a similar fashion, we found that the height of the first vortex was 25 mm, which corresponded to a vortex formation time of 0.011 s (with an exit velocity of 2.41 m/s). Therefore, the swirling frequency inferred from the reconstruction was 91 Hz, which was in agreement with actual flame settings.

Finally, we examine the reprojection errors and experimental reconstruction residual for diffusion jet flame and swirl flame, and the results are shown in Fig. 14. Since the ground truths of the experimental flames are unknown, we use reprojection error (the difference between measurements and calculated projections from the reconstruction) to test the reconstruction accuracy of algorithms and still use the residual as the convergence performance indicator. Essentially, these two quantities are correlated with each other. A comparable tendency can be found for SART and SNNART algorithms from the experimental results. More specifically, the SNNART algorithm converges faster and yields a smaller residual than SART realization. If we keep in mind
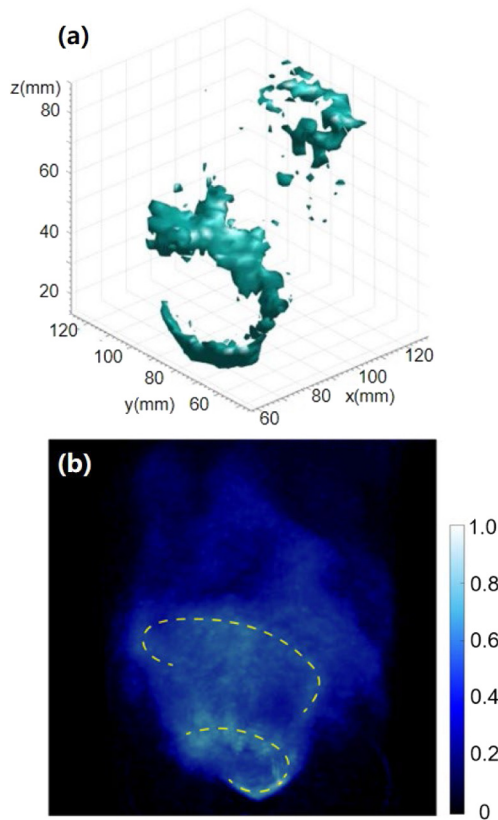
Fig. 13. Combustion physics interpretation from the 3D flame reconstruction. Panel (a). Iso-surface plot representing the flame structure. Panel (b). Vortexing structure within the flame reconstruction.
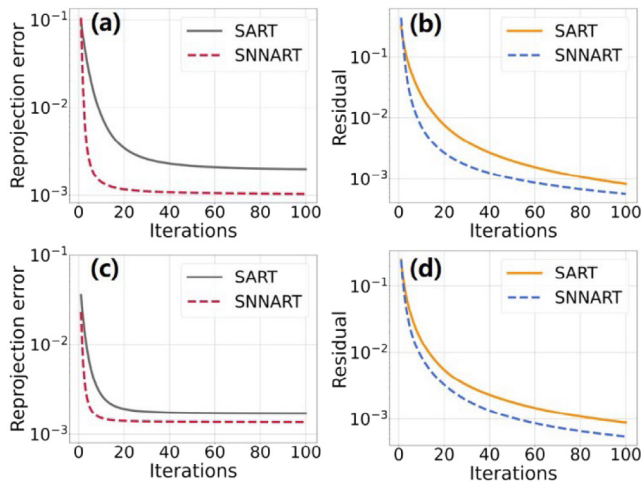

Fig. 14. Reconstruction capabilities using SART and SNNART algorithms. Panel (a). Jet flame, reprojection error as a function of iterations. Panel (b). Jet flame, reconstruction residual as a function of iterations. Panel (c). Swirl flame, reprojection error as a function of iterations. Panel (d). Swirl flame, reconstruction residual as a function of iterations.

that SNNART and SART are based on very similar formulas (x_v as the variable for SART and $x_v^{1/2}$ for SNNART), the results in Fig. 14 indicate that the SNNART indeed converges to a better point (although could be local minima as well) than SART reconstruction, and the flame reconstructions obtained by SNNART could be more credible than those obtained using SART, given the capacity of streak-suppressing is considered.

4. Conclusions

In this investigation, we proposed a CTC realization with improved calibration means which uses a cylindrical ChArUco as the calibration target, and the relative position constraints of cameras were used to improve the calibration accuracy. Based on the calibration results, the weight matrix was calculated based on a sub-voxel projection method in a parallel computing way. Then a non-negative algebraic reconstruction technique (NNART) was analytically derived and implemented, with its parallel computing form SNNART. The algorithm is then verified and validated by a numerical jet flame and two experimental flames with different complexity. The results show that NNART and SNNART algorithms can successfully suppress streaks or other related reconstruction glitches, thus yielding a better reconstruction quality and faster convergence speed. Experimental reconstructions also illustrated detailed flame structures and unique flame patterns, which is quite useful for reactive flow studies and theoretical investigations in providing a precise three-dimensional flame emission distribution.

Declaration of competing interest

The authors declare that they have no known competing financial interests or personal relationships that could have appeared to influence the work reported in this paper.

Acknowledgments

References

[1] W. Cai, C.F. Kaminski, Tomographic absorption spectroscopy for the study of gas dynamics and reactive flows, Prog. Energy Combust. Sci. 59 (2017) 1–31.

[2] J. Floyd, P. Geipel, A.M. Kempf, Computed tomography of chemiluminescence (CTC): Instantaneous 3D measurements and Phantom studies of a turbulent opposed jet flame, Combust. Flame 158 (2011) 376–391.

[3] Z. Niu, H. Qi, J. Shi, J. Zhang, Y. Ren, Temperature field reconstruction of 3D luminous flames based on light field tomography theory, Sci. Chin. Technol. Sci. 64 (2020) 223–236.

[4] X. Li, L. Ma, Volumetric imaging of turbulent reactive flows at khz based on computed tomography, Opt. Express 22 (2014).

[5] A.G. Gaydon, The Spectroscopy of Flames, Wiley London, New York,Chapman, New York ,London, 1957.

[6] J. Wang, Y. Song, Z.H. Li, A. Kempf, A.Z. He, Multi-directional 3D flame chemiluminescence tomography based on lens imaging, Opt. Lett. 40 (2015) 1231–1234.

[7] X. Wan, W. Xiong, Z. Zhang, F. Chang, An online emission spectral tomography system with digital signal processor, Opt. Express 17 (2009) 5279.

[8] J. Floyd, A.M. Kempf, Computed tomography of chemiluminescence (CTC): High resolution and instantaneous 3-D measurements of a matrix burner, Proc. Combust. Inst. 33 (2011) 751–758.

[9] Y. Jin, Y. Song, X. Qu, Z. Li, Y. Ji, A. He, Three-dimensional dynamic measurements of CH* and C2* concentrations in flame using simultaneous chemiluminescence tomography, Opt. Express 25 (2017) 4640.

[10] Z. Zhang, A flexible new technique for camera calibration, IEEE Trans. Pattern Anal. Mach. Intell. 22 (2000) 1330–1334.

[11] J. Wang, W. Zhang, Y. Zhang, X. Yu, Camera calibration for multidirectional flame chemiluminescence tomography, Opt. Eng. 56 (2017) 041307.

[12] X. Li, L. Ma, Capabilities and limitations of 3D flame measurements based on computed tomography of chemiluminescence, Combust. Flame 162 (2015) 642–651.

[13] L. Thomas, B. Tremblais, L. David, Optimization of the volume reconstruction for classical tomo-PIV algorithms (MART, BIMART and SMART): synthetic and experimental studies, Meas. Sci. Technol. 25 (2014).

[14] D. Schanz, S. Gesemann, A. Schröder, B. Wieneke, M. Novara, Non-uniform optical transfer functions in particle imaging: calibration and application to tomographic reconstruction, Meas. Sci. Technol. 24 (2013).

[15] H. Pan, D. Xiao, F. Zhang, X. Li, M. Xu, Adaptive weight matrix and phantom intensity learning for computed tomography of chemiluminescence, Opt. Express 29 (2021).

[16] H. Pan, F. Zhang, X. Li, M. Xu, Learning implicit light propagation from multi-flame projections for computed tomography of chemiluminescence, Appl. Opt. 60 (2021).

[17] R. Gordon, A tutorial on art (algebraic reconstruction techniques), IEEE Trans. Nucl. Sci. 21 (1974) 78–93.

[18] A.H. Andersen, Algebraic reconstruction in CT from limited views, IEEE Trans. Med. Imaging 8 (1989) 50–55.

[19] A.H. Andersen, A.C. Kak, Simultaneous algebraic reconstruction technique (SART): A superior implementation of the Art algorithm, Ultrason. Imaging 6 (1984) 81–94.

[20] D. Verhoeven, Limited-data computed tomography algorithms for the physical sciences, Appl. Opt. 32 (1993) 3736.

[21] G. Elsinga, F. Scarano, B. Wieneke, B. Oudheusden, Tomographic particle image velocimetry, Exp. Fluids 41 (2006) 933–947.

[22] C. Atkinson, J. Soria, An efficient simultaneous reconstruction technique for tomographic particle image velocimetry, Exp. Fluids 47 (2009) 553–568.

[23] F. Meierhofer, L. Mädler, U. Fritsching, Nanoparticle evolution in flame spray pyrolysis—Process design via experimental and computational analysis, AIChE J. 66 (2019).

[24] H. Liu, G. Paolillo, T. Astarita, C. Shui, W. Cai, Computed tomography of chemiluminescence for the measurements of flames confined within a cylindrical glass, Opt. Lett. 44 (2019) 4793–4796.

[25] J. Heikkila, O. Silven, A four-step camera calibration procedure with implicit image correction, 1997, pp. 1106–1112.

[26] G. Bradski, A. Kaehler, Learning OpenCV: Computer Vision with the OpenCV Library, O'Reilly Media, Sebastopol, 2008, Incorporated.

[27] F.J. Romero-Ramirez, R. Muñoz Salinas, R. Medina-Carnicer, Speeded up detection of squared fiducial markers, Image Vis. Comput. 76 (2018) 38–47.

[28] S. Garrido-Jurado, R. Muñoz Salinas, F.J. Madrid-Cuevas, R. Medina-Carnicer, Generation of fiducial marker dictionaries using mixed integer linear programming, Pattern Recognit. 51 (2016) 481–491.

[29] A. Gwon Hwan, L. Siyeong, Y. Min-Woo, Y. Kugjin, C. Won-Sik, K. Suk-Ju, Charuco board-based omnidirectional camera calibration method, Electronics (Basel) 7 (2018) 421.

[30] D. Hu, D. DeTone, V. Chauhan, I. Spivak, T. Malisiewicz, Deep ChArUco: Dark ChArUco marker pose estimation, 2018.

[31] Y. Zheng, S. Sugimoto, M. Okutomit, ASPnP: An accurate and scalable solution to the perspective-n-point problem, IEICE Trans. Inf. Syst. E96D (2013) 1525–1535.

[32] A. Paszke, S. Gross, F. Massa, A. Lerer, J. Bradbury, G. Chanan, T. Killeen, Z. Lin, N. Gimelshein, L. Antiga, A. Desmaison, A. Köpf, E. Yang, Z. DeVito, M. Raison, A. Tejani, S. Chilamkurthy, B. Steiner, L. Fang, J. Bai, S. Chintala, PyTorch: An imperative style, high-performance deep learning library, 2019.

[33] D.P. Kingma, J. Ba, Adam: A method for stochastic optimization, 2014.

[34] R.M. Rangayyan, R. Gordon, Streak preventive image reconstruction with ART and adaptive filtering, TMI 1 (1982) 173–178.

[35] Z. Wang, A.C. Bovik, H.R. Sheikh, E.P. Simoncelli, Image quality assessment: From error visibility to structural similarity, TIP 13 (2004) 600–612.

[36] A.M. Steinberg, C.M. Arndt, W. Meier, Parametric study of vortex structures and their dynamics in swirl-stabilized combustion, Proc. Combust. Inst. 34 (2013) 3117–3125.